P4.7 ENTRAINMENT INTO SHEARED CONVECTIVE BOUNDARY LAYERS AS PREDICTED BY DIFFERENT LARGE EDDY SIMULATION CODES

Evgeni Fedorovich* and Robert Conzemius
School of Meteorology, University of Oklahoma, Norman, Oklahoma

Igor Esau
Nansen Environmental and Remote Sensing Center, Bergen, Norway

Fotini Katopodes Chow
Environmental Fluid Mechanics Laboratory, Stanford University, California

David Lewellen
Department of Mechanical and Aerospace Engineering, West Virginia University, Morgantown, West Virginia

Chin-Hoh Moeng and Peter Sullivan
National Center for Atmospheric Research, Boulder, Colorado

David Pino
Institute for Space Studies of Catalonia and Department of Applied Physics, Technical University of Catalonia, Barcelona, Spain

Jordi Vilà-Guerau de Arellano
Department of Meteorology and Air Quality, Wageningen University, Netherlands

1. INTRODUCTION

Entrainment is a complex physical process that is a driving mechanism of convective boundary-layer (CBL) development. There is no consensus in the boundary-layer research community regarding the role played by wind shears in the entrainment dynamics. Previous numerical studies of sheared CBLs primarily focused on the turbulence regimes associated with quasi-stationary CBL evolution. In these studies, convective entrainment and its influence on CBL growth dynamics were not regarded as main research issues. In the present study, the emphasis is specifically laid on the characteristics of entrainment related to the CBL growth.

Some previously suggested theories (e.g., Hunt and Durbin 1999), pointed to possible attenuation of vertical turbulent transport across the sheared entrainment layer that could lead to the reduction of entrainment. On the other hand, most numerical studies conducted to date (e.g., Fedorovich et al. 2001b; Pino et al. 2003) have found overall enhancement of entrainment and CBL growth with surface and/or elevated wind shear, yet others (e.g, Conzemius and Fedorovich 2002) have not. Because of these different results, this comparison exercise seeks to explore any differences in the predicted entrainment in sheared CBLs that may be code-dependent, and with this goal in mind, we have brought together several numerical codes built on the large-eddy simulation (LES) methodology in an attempt to investigate basic features of entrainment dynamics in sheared CBLs as reproduced by LES codes of different architecture, with different numerical algorithms, of different spatial and temporal resolution, and employing different subgrid-turbulence and surface-layer parameterizations.

* *Corresponding author address:* Evgeni Fedorovich, School of Meteorology, University of Oklahoma, 100 East Boyd, Norman, OK 73019-1013;
e-mail: fedorovich@ou.edu

2. LES COMPARISON EXERCISE

All participating LES codes used a simulation domain of $X \times Y \times Z = 10 \times 10 \times 2$ km^3 (slight deviations from these basic dimensions were allowed) with periodic lateral boundary conditions. Three atmospheric CBL cases were reproduced with the same surface virtual potential temperature flux (0.1 K m/s) and the same thermal stratification in the free atmosphere above the CBL (0.003 K/m), but with different shear forcings. The following wind-shear configurations were studied:

1. No mean shear (**NS** case), which was the reference case.
2. Height-constant geostrophic wind of 20 m/s magnitude throughout the whole simulation domain (**GC** case).
3. Geostrophic wind, which linearly increases from zero at the surface to 20 m/s at the domain top (**GS** case).

The geostrophic wind included only the longitudinal (x) component u_g, so the y component of the geostrophic wind, v_g, was set equal to zero. For all simulated cases,

the surface roughness length, geographic latitude, and reference temperature were prescribed to be 0.01 m, 40° N, and 300 K, respectively.

In the initial-flow configurations set for the exercise (see Fig. 1), virtual potential temperature θ changed vertically at a constant rate of 0.003 K/m throughout the entire domain starting from the surface. The initial wind velocity in the domain was geostrophic (zero in the **NS** case), with the vertical velocity component set equal to zero.

Numerical grids, discretization methods, time advancement schemes, convection initiation procedures, subgrid-turbulence closures, and boundary conditions at the bottom and at the top were code-specific (see section 3 for the code descriptions).

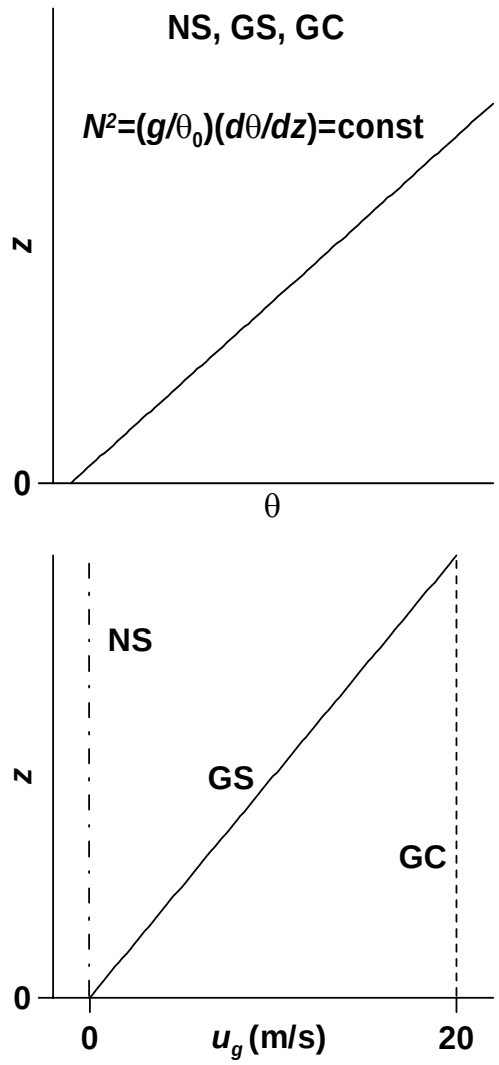

Figure 1. Initial profiles of the virtual potential temperature θ and x component of the geostrophic wind velocity, u_g, for the simulated CBL cases.

Turbulence statistics were calculated every 200 seconds. In order to avoid uncertainties associated with complementary time averaging, the averaging (denoted hereafter by overbar) was performed over horizontal planes only. Also, to minimize spurious effects associated with upper boundary conditions and ensure a sufficiently large ratio between the width of the domain and the depth of the simulated CBL, only the data from simulated CBLs shallower than 1200 m in depth (60% of the domain depth and 12% of the domain width) were used. A large domain-width to CBL-depth ratio is particularly important for the sheared CBL because of the roll-like turbulent structures contained therein. Small CBL aspect ratios can lead to under-sampling of the flow fields for the calculation of turbulence statistics.

The following statistics were calculated (deviations from horizontal-plane means are denoted by primes).

I. First-order statistics:

$\overline{\theta}$, mean virtual potential temperature,

$\overline{u}$ and $\overline{v}$, mean x and y velocity components.

II. Second-order statistics:

$\overline{w'\theta'}$, vertical kinematic heat flux (resolved and subgrid).

$\overline{w'u'}$ and $\overline{w'v'}$, components of vertical turbulent momentum flux (resolved and subgrid).

$\overline{u'u'}$, $\overline{v'v'}$, $\overline{w'w'}$, velocity component variances (resolved and subgrid),

$\overline{\theta'\theta'}$, virtual potential temperature variance (resolved).

III. Third-order statistics:

$\overline{w'w'w'}$, third moment of vertical velocity (resolved),

$\overline{\theta'\theta'\theta'}$, third moment of virtual potential temperature (resolved).

The CBL depth z_i was determined from the $\overline{\theta}$ and $\overline{w'\theta'}$ (total = resolved + subgrid) data by two methods: either by taking z_i as the height of the heat flux minimum within the entrainment zone, or assigning z_i to the level of maximum temperature gradient within the inversion layer at the CBL top. As shown in Sullivan et al. (1998) and discussed in Fedorovich et al. (2004) these two methods are expected to provide somewhat different CBL depth estimates.

3. LES CODES

The following research teams, using six different LES codes, participated in the comparison study:

1. School of Meteorology, University of Oklahoma (**OU**), USA (Evgeni Fedorovich and Robert Conzemius).
2. Mesoscale and Microscale Meteorology Division of National Center for Atmospheric Research (**NCAR**), Boulder, Colorado, USA (Chin-Hoh Moeng and Peter Sullivan).

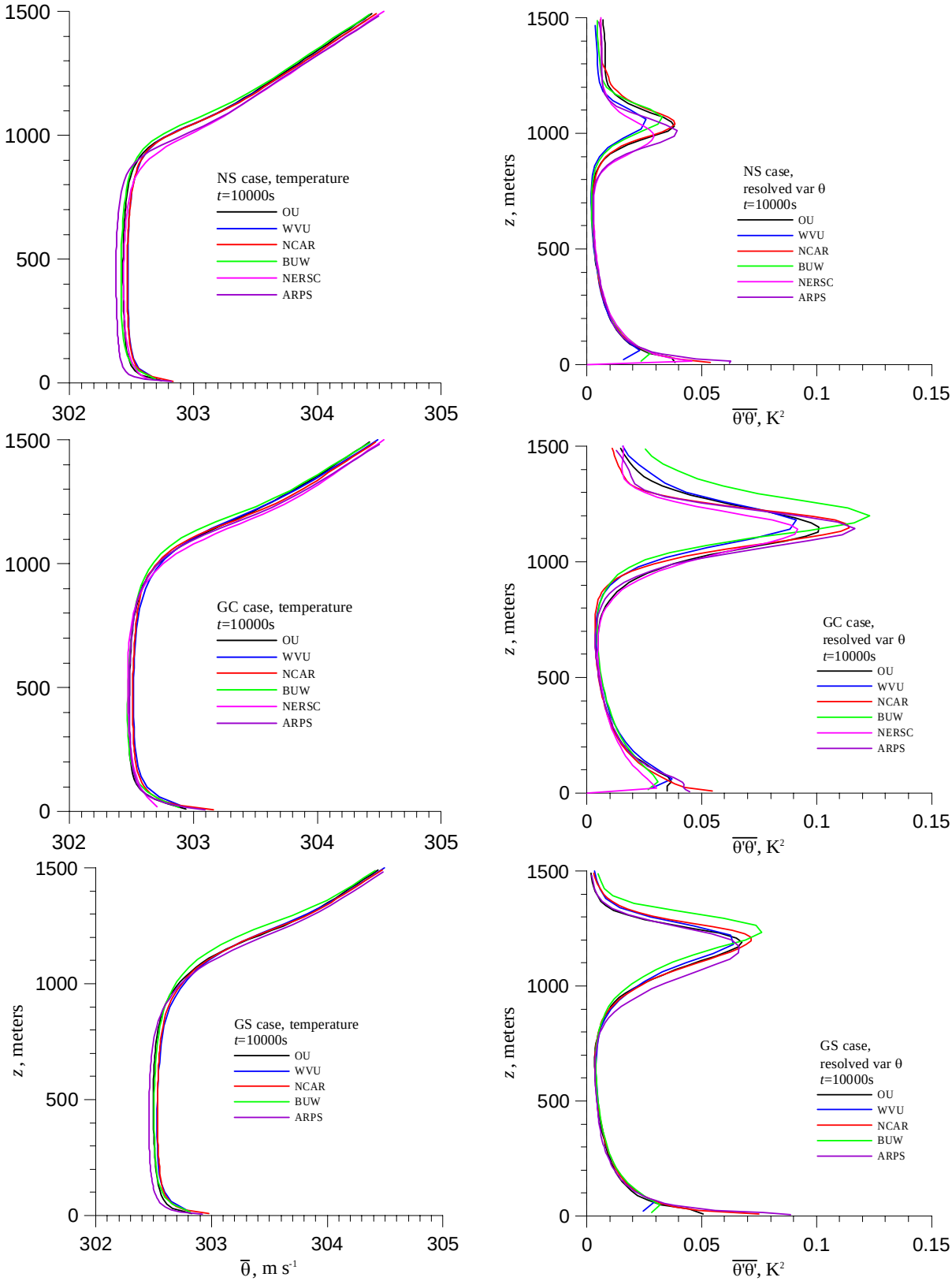

Figure 2. Profiles of the mean virtual potential temperature (right-hand plots) and resolved temperature variance (left-hand plots) for all three simulated cases (**NS**, **GC**, and **GS**, see section 2) at *t*=10000s.

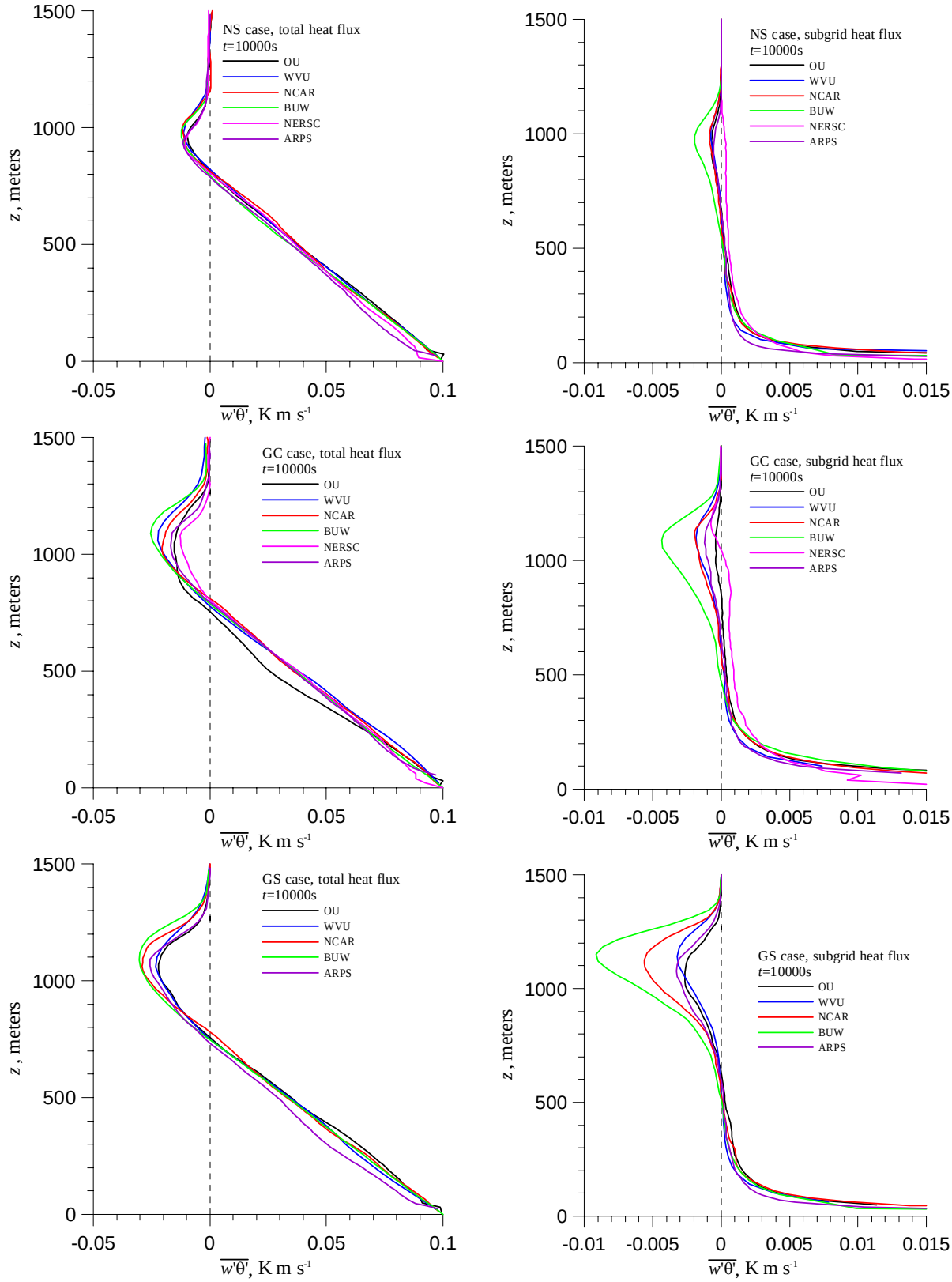

Figure 3. Vertical kinematic heat flux (left-hand plots: total=resolved+subgrid; right-hand plots: subgrid) for all three simulated cases (**NS**, **GC**, and **GS**, see section 2) at *t*=10000s.

3. Department of Mechanical and Aerospace Engineering, West Virginia University (**WVU**), Morgantown, West Virginia, USA (David Lewellen).
4. Nansen Environmental and Remote Sensing Center (**NERSC**), Bergen, Norway (Igor Esau).
5. Environmental Fluid Mechanics Laboratory, Stanford University, California, USA. Fotini Katopodes Chow used a LES version of the Advanced Regional Prediction System (**ARPS**, Xue et al. 2000, 2001).
6. Joint team of the Institute for Space Studies of Catalonia, Barcelona, Spain (David Pino) and Department of Meteorology and Air Quality, Wageningen University, Netherlands (Jordi Vilà-Guerau de Arellano). Their LES code is denoted **BUW**.

3.1 *University of Oklahoma (OU)*

The **OU** LES code, described in Fedorovich et al. (2001a), employed a finite-difference discretization of filtered equations of atmospheric dynamics and thermodynamics on a 256×256×100 staggered grid with spacing of $\Delta x = \Delta y = 40\text{m}$ and $\Delta z = 20\text{m}$. Basic features of the **OU** code are as follows:

- leap-frog scheme with weak Asselin filter for time advancement;
- centered second-order approximations for the advection and diffusion terms of the filtered transport equations;
- pressure calculated diagnostically from the Poisson equation solved by combining the Fast Fourier Transform (FFT) technique (in *x* and *y* directions) and tri-diagonal matrix (TDM) inversion (over *z*);
- Deardorff (1980) subgrid closure, based on a prognostic equation for the subgrid turbulence kinetic energy (STKE);
- sponge layer in the upper 20% of domain to damp reflections;
- Monin-Obukhov similarity relationships in the near-surface region of the CBL applied locally to relate one-point dynamic and thermal parameters of the flow at the surface;
- turbulent convection initiated by random temperature perturbations in the first grid-cell layer adjacent to the surface.

3.2 *National Center for Atmospheric Research (NCAR)*

The **NCAR** code, described in Moeng (1984) and Sullivan et al. (1994), was run on a 250×250×128 vertically staggered grid with a uniform vertical spacing Δz of 15.6 m and truncation of the resolved-scale flow fields in *x* and *y* directions at a wavelength of 80m. Non-staggered spacing was used in both horizontal directions. Basic features of the **NCAR** code are as follows:

- third-order Runge-Kutta scheme is used for integration over time;
- mixed pseudospectral (along horizontal planes) and second order finite-difference (in the vertical direction) spatial discretization;
- pressure is calculated diagnostically from the Poisson equation solved using the FFT-TDM technique (see section 3.1);
- two-part eddy viscosity turbulence model (Sullivan et al. 1994) to parameterize subgrid turbulent stresses;
- radiation boundary conditions for resolved horizontal velocity components and zero STKE at the domain top;
- employed subgrid closure in conjunction with lower boundary condition provides for transition from LES to ensemble-averaging modeling as the underlying surface is approached and matches the velocity derivative near the surface to the Monin-Obukhov similarity relation independent of grid resolution; this makes the subgrid closure scheme less dissipative close to the surface and leads to more resolved turbulence in this flow region.

3.3 *West Virginia University (WVU)*

The basic equations of the **WVU** code are summarized in Sykes and Henn (1989) and Lewellen and Lewellen (1998). For the exercise, the code was run on a grid with uniform horizontal spacing of 39m and uniform vertical spacing of 40m. Basic features of the **WVU** code are as follows:

- time integration is performed by a leapfrog scheme;
- momentum transport equations are discretized with a second-order finite-difference scheme on a staggered grid; scalars are advected using a monotone scheme based on the piecewise parabolic method.
- Poisson equation for pressure is solved by the FFT-TDM technique (see section 3.1);
- subgrid turbulence parameterization is based on a simplified version of the ARAP second-order quasi-equilibrium closure model (Sykes and Henn 1989), in which STKE is the primary prognostic variable and the subgrid turbulence length scale is limited by the local grid spacing, stability, and distance from the surface;
- turbulent fluxes at the underlying surface are evaluated using Monin-Obukhov similarity relationships;

3.4 *Nansen Environmental and Remote Sensing Center (NERSC)*

The **NERSC** code, presented in Esau (2004), is based on a fully conservative central difference numerical scheme. The code was run on a staggered 256×256×128 grid with horizontal spacing of $\Delta x = \Delta y = 40\text{m}$ and vertical spacing of $\Delta z = 20\text{m}$. Basic features of the **NERSC** code are as follows:

- filtered prognostic equations are integrated in time using fourth-order Runge-Kutta scheme;

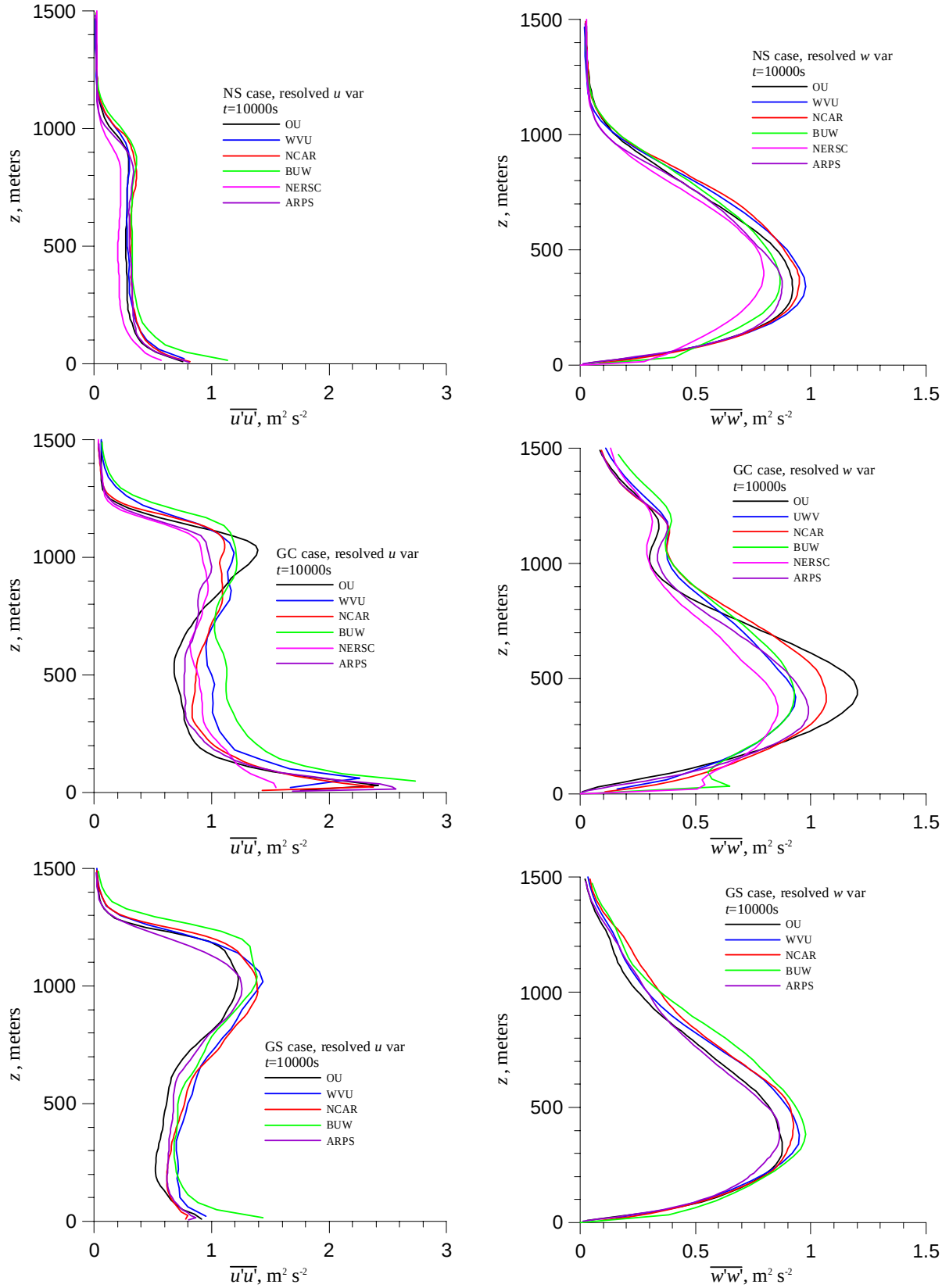

Figure 4. Variances of the resolved *u* (left-hand plots) and *w* (right-hand plots) velocity components for all three simulated cases (**NS**, **GC**, and **GS**, see section 2) at *t*=10000s.

- nonlinear advection is discretized in a skew-symmetric form with no limiters applied to compensate for non-monotonic behavior of the advection scheme;
- dynamic mixed subgrid (subfilter) turbulence model in the formulation of Vreman et al. (1994) is employed: shear stress is split in the scale-similarity and eddy viscosity parts with one free parameter (turbulence length scale), which is evaluated by minimization of the discrepancy between the actual and parameterized stress expressed in terms of filtered flow variables;
- at the top of simulation domain, Neumann (zero-gradient) conditions are prescribed for the resolved horizontal velocity components and resolved temperature, while the resolved vertical velocity is set equal to zero.

3.5 *Institute for Space Studies of Catalonia / Wageningen University (BUW)*

The LES code of **BUW** is described in Cuijpers and Duynkerke (1993) and Cuijpers and Holtslag (1998). Its application to the simulation of sheared CBL is demonstrated in Pino et al. (2003). The code uses finite-difference versions of the filtered momentum (written in the Boussinesq approximation) and heat transport equations on a staggered grid. A 256×256×64 grid with spacing $\Delta x = \Delta y = 39.1\text{m}$ and $\Delta z = 32\text{m}$ was used for this exercise.

The **BUW** code is a close relative of the **OU** code (section 3.1). It differs from the latter with respect to

- advection scheme (a monotone kappa scheme is used in the **BUW** code for advection of scalars);
- choice of some constants in the subgrid turbulence parameterizations;
- application of Monin-Obukhov similarity relationships at the surface.

3.6 *Atmospheric Regional Prediction System (ARPS) / Stanford University*

The **ARPS** code (Xue et al. 2000, 2001) was developed at the Center for Analysis and Prediction of Storms at the University of Oklahoma.

The LES version of **ARPS** used in the present study was run on a 259×259×103 staggered grid with uniform spacing of 40m×40m in the horizontal. In the vertical, a stretched grid was used, with 10-m spacing at the bottom of domain and 30-m spacing at the domain top with an average spacing of 20 m. Basic features of the employed version of **ARPS** are as follows:

- filtered equations of atmospheric dynamics and thermodynamics are solved numerically in the non-hydrostatic, compressible form;
- integration over time is performed with a mode-splitting technique designed to accommodate high-frequency acoustic waves: the large time steps (0.5 s) use the leapfrog method, while a first-order forward-backward scheme is employed for the small time steps (0.05 s), except for the terms responsible for vertical acoustic-wave propagation, which are treated implicitly;
- fourth-order spatial differencing for advection;
- Deardorff (1980) STKE subgrid closure;
- Rayleigh damping applied in the upper portion of numerical domain to minimize reflection from the rigid-lid boundary at the domain top;
- Monin-Obukhov similarity applied at the surface;
- random initial temperature perturbations with r.m.s. value of 2K to initiate convection.

5. SIMULATED FLOW CHARACTERISTICS

As could be expected, all codes predict evolution of the mean CBL temperature field in a rather close manner, see Fig. 2. The agreement between the codes is especially good for the temperature profiles in the **GC** case. In the **NS** and **GS** case, the divergence between the predicted profiles is slightly more noticeable, particularly in the vicinity of the capping inversion (its location can be deduced from the maximum vertical temperature gradient), whose height shows minor variations as predicted by different codes. All codes predict, in a similar manner, a more elevated capping inversion (and thus the larger CBL thickness—see the discussion in Section 6) in both sheared CBL cases (**GC** and **GS**) relative to the shear-free case. The maxima in the temperature variance distributions (also shown in Fig. 2) are approximately collocated, with predictions of these maxima falling within 200 m of one another for all simulated cases. In both sheared CBL cases, the **BUW** code predicts the largest temperatures variances and the highest inversion position.

The LES data on the vertical kinematic heat flux, shown in Fig. 3, are qualitatively consistent with the mean temperature and temperature variance distributions. We show the total (resolved+subrid) heat flux and subgrid flux separately in this figure to highlight areas where the subgrid flux is a significant contributor to the total. One may notice that the largest subgrid contribution is located in the near-surface region of the CBL, and this contribution is reproduced in a similar manner by all participating codes. The depth of this near-surface region is slightly larger in the presence of surface shears and appears to depend on the mean shear magnitude (it is largest in the **GC** case, see Fig. 6).

Another region of enhanced subgrid flux is located within the entrainment layer (it is marked by negative heat flux values). Here, the different codes predict rather different values of subgrid flux, up to 30% of the total flux magnitude in some cases. Wind shear across the entrainment layer (which is the strongest in the **GS** case) is definitely a factor attributing more heat flux to the subgrid-scale motions. The relatively small subgrid flux values predicted by the **OU** code in the entrainment layer may be a symptom of numerical damping of high-wavenumber turbulent fluctuations by the time-integration scheme. This damping, which becomes worse in faster flow, attenuates energy transfer to the subgrid motions at high-wavenumber intervals of turbulence spectra.

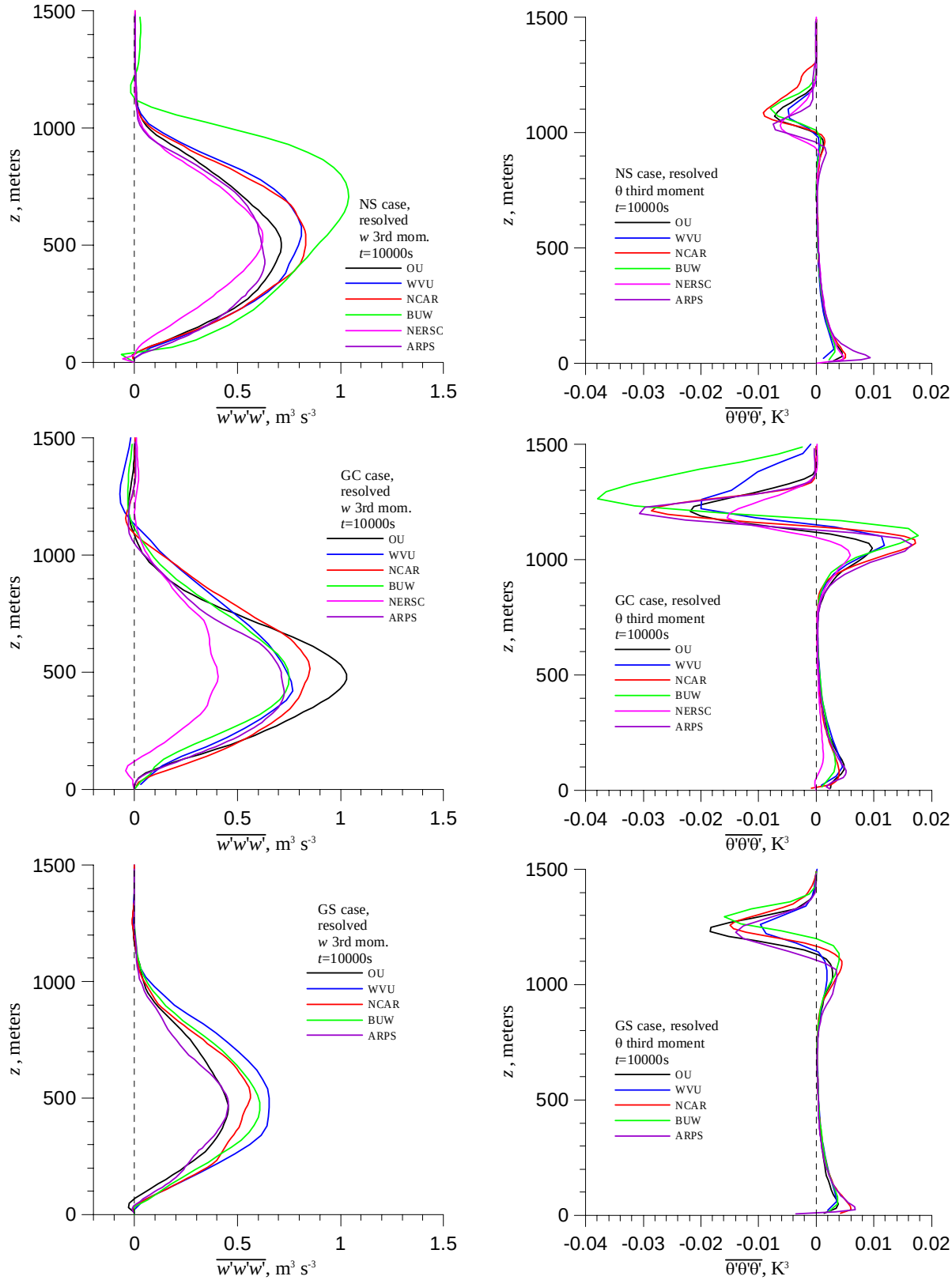

Figure 5. Third moments of the resolved vertical velocity (left-hand plots) and virtual potential temperature (right-hand plots) for all three simulated cases (**NS**, **GC**, and **GS**, see section 2) at *t*=10000s.

The smallest deviations between the total heat flux profiles predicted by different codes are observed in the shear-free case (**NS**). All codes predict the increase of the entrainment-zone depth and magnitude of the entrainment heat flux in sheared CBLs (**GC** and **GS** cases). Deeper heat flux minima in the **GS** case indicate that the entrainment zone shear may play the leading role in the entrainment enhancement. The latter conclusion, however, should be treated with caution because analyzed statistics are representative only of one time moment in the simulation.

Horizontal (*u* component) and vertical (*w* component) velocity variances presented in Fig. 4 show rather small code-to-code variability given the fact that they were not processed through any kind of temporal averaging. Only the resolved velocity statistics are presented in the figure. The compilation of the subgrid variance data is not yet completed. Effects of shear on the CBL turbulence are seen in the presented velocity variances rather vividly. As can be expected, the horizontal velocity variance is significantly larger throughout the depth of the CBL in the cases with mean shear. Secondary maxima appear in the *u* variance distributions within sheared entrainment layers (**GC** and **GS** cases) at heights approximately corresponding to the levels of maximum mean shear. In the **GS** case, the vertical velocity variance is larger in the entrainment zone than it is in the **NS** case, but its profile in the middle of the CBL looks qualitatively similar to the **NS** profile.

On the other hand, for the **GC** case, the *w* component variance is larger throughout most of the CBL than it is in either the **NS** or **GS** cases. In general, vertical velocity fluctuations in the sheared CBLs retain much higher values throughout the entrainment zone than in the **NS** case, and their rather rapid decay towards the CBL top in the latter case is replaced either by a more gradual decrease (profile bend) in the **GS** case or a slight increase (development of a secondary maximum) in the **GC** case. Remarkably, both the bend and secondary maximum of $\overline{w'w'}$ profiles are shifted upwards with respect to the maxima in the $\overline{u'u'}$ profiles and the heat flux minima (see Fig. 3).

Such modifications of the CBL vertical velocity variance in the presence of elevated shears appear to be rather consistent features of the conducted simulations. However, it is not clear at this point what physical mechanisms might be responsible for these modifications. Also, the presence of elevated shear, which is stronger in the **GS** case, modifies the turbulence structure in the entrainment zone. Strong surface shear tends to modify the turbulence structure throughout the entire depth of the CBL. This may be related to the transport of the surface-shear generated turbulence by buoyantly forced turbulence. In the **GC** case, with the strongest surface shear, the enhancement of vertical velocity fluctuations in the middle of the CBL is clearer, but the **GC** case also develops shear across the CBL top as the mixed layer momentum slows, so qualitatively similar modifications to the turbulence structure in the entrainment zone occur in the **GC** and **GS** cases. Nevertheless, the enhancement of vertical velocity fluctuations in the interior of the CBL in the **GC** case seem to be heavily code-dependent, so it is difficult to make any definitive conclusion regarding the modification of the turbulence regime there.

The third-order moments of vertical velocity and virtual potential temperature fluctuations, shown in Fig. 5, exhibit a stronger code-to-code variability. This is not a surprising behavior, given that these statistics have been calculated by horizontal averaging only. Despite this fact, all codes capture certain features of the CBL turbulence structure under the influence of shear in a common manner.

First of all, all the codes agree on the change of sign of $\overline{\theta'\theta'\theta'}$ in the middle of the entrainment zone. The temperature fluctuations are positively skewed in the lower portion of the entrainment zone, just beneath the capping inversion, and become strongly negatively skewed in the upper portion of the entrainment zone, where the magnitude of $\overline{\theta'\theta'\theta'}$ is several times larger than in the layer just below the inversion.

Generally, the third moments of a random variable characterize the asymmetry of its distribution and thus the proportion between the ranges of its positive and negative fluctuations. With respect to the analyzed data, this means that, within the lower portion of the entrainment zone, warm air transported by thermals occupies a smaller fraction of the horizontal area than does the cooler ambient air. These narrow thermals overshoot their equilibrium level and, as indicated by the change of sign of $\overline{\theta'\theta'\theta'}$ at the inversion level, they become cooler than their surroundings in the upper portion of the entrainment zone. The amplitude of the $\overline{\theta'\theta'\theta'}$ variations across the entrainment layer is the largest in the **GC** case, while in the absence of mean shear (**NS** case), these variations are comparatively small. However, the amplitude seems to have no direct relation to the magnitude of shear across the entrainment zone: the magnitude of elevated shear is much larger in the **GS** case than in the **GC** case (see Fig. 6).

Vertical distributions of $\overline{w'w'w'}$ characterize the vertical turbulent transport of turbulence kinetic energy throughout the CBL. In all three simulated cases, the $\overline{w'w'w'}$ values are positive over the main portion of the CBL, and therefore, the energy transport is directed upwards. This also means that, with the exception of the shallow near-surface region and the entrainment zone, the upward motions with positive values of *w'* are narrower but have larger magnitudes than descending motions with negative *w'*. In the vicinity of the surface, however, the values $\overline{w'w'w'}$ are either slightly negative (as predicted by some of the codes) or do not deviate significantly from zero (as other codes predict). This suggests that in the near-surface region of the CBL flow, densely packed rising plumes are separated by downdrafts, which are narrower but faster than the plumes or at least statistically equivalent to them.

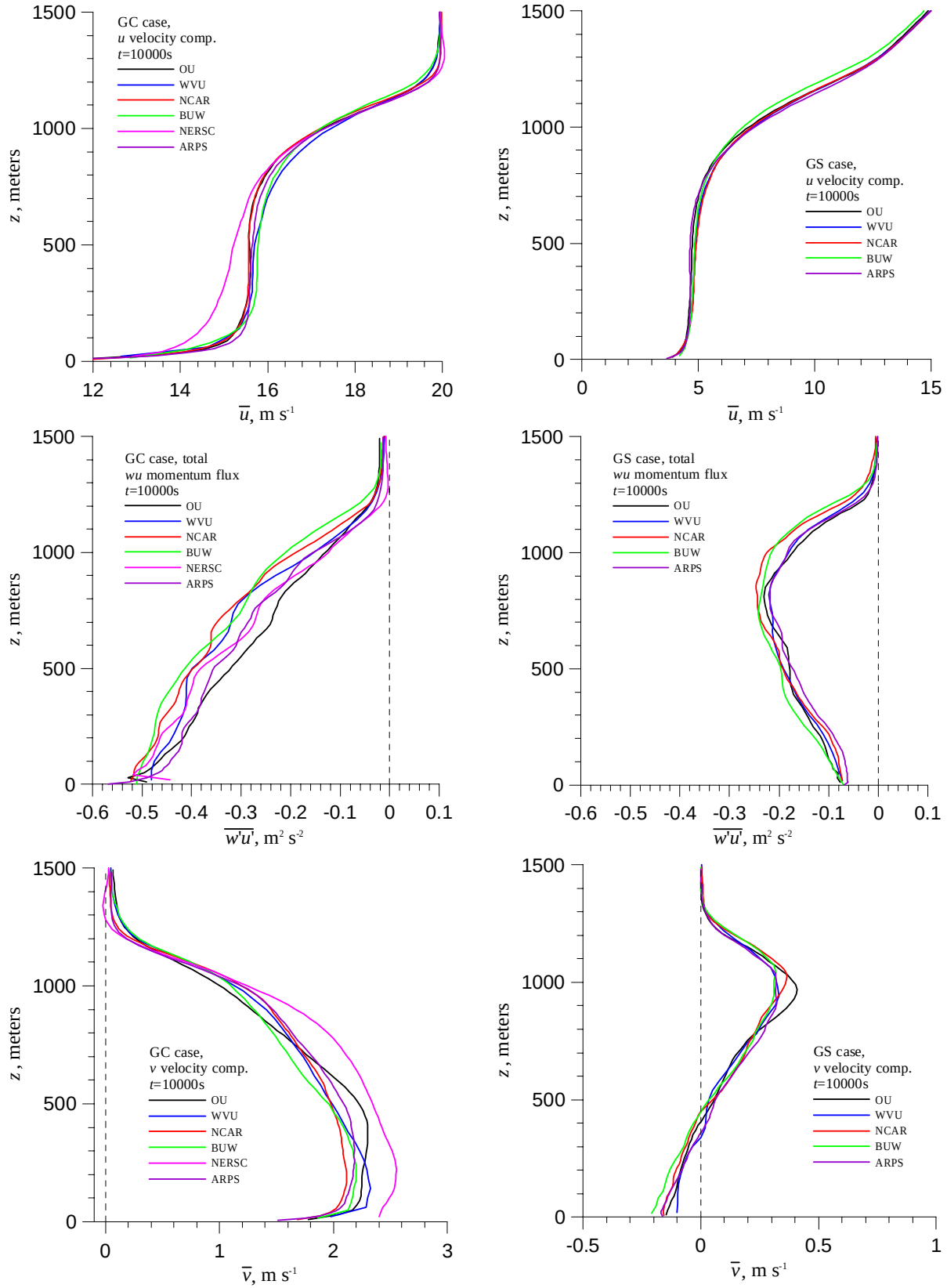

Figure 6. Mean *u* component (top), *x* component of vertical momentum flux normalized by density (middle), and mean *v* component (bottom) for the **GC** (left-hand plots) and **GS** (right-hand plots) cases (see section 2) at *t*=10000s.

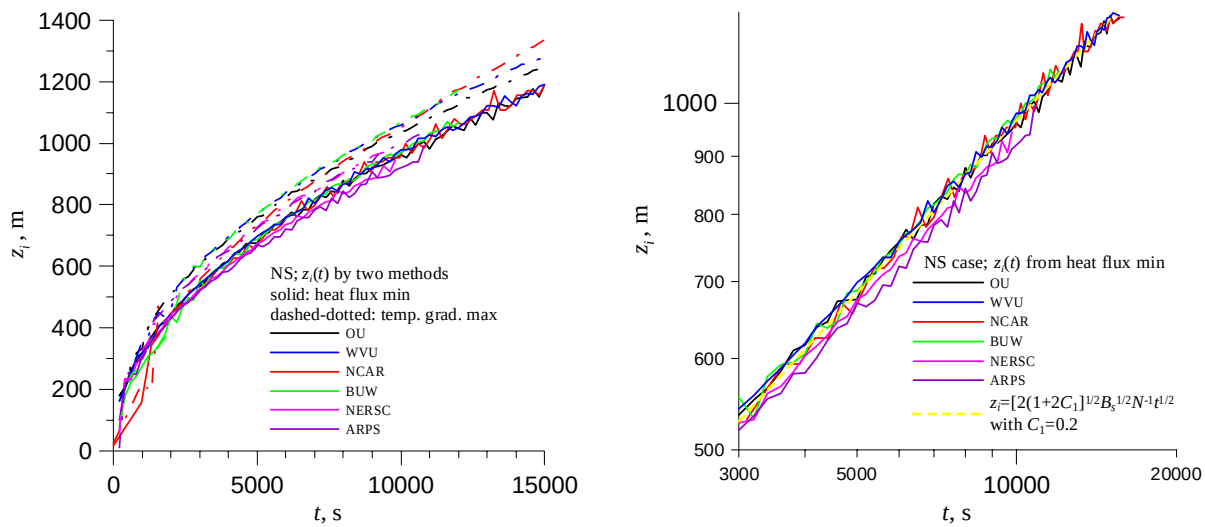

Figure 7. Computed z_i (t) for the **NS** case (left-hand [plot) and its verification at large t against analytical zero-order prediction (right-hand plot).

Throughout the entrainment zone, the values of $\overline{w'w'w'}$ are typically close to zero or slightly negative. In some cases, however (see $\overline{w'w'w'}$ profiles for the **GC** case), $\overline{w'w'w'}$ can become noticeably negative, which could possibly be an indication of narrow sweeping downward motions associated with the breaking of Kelvin-Helmholtz billows at the sheared density interface (temperature inversion).

Contribution of these motions to the entrainment could be a reason for larger entrainment heat flux values in the **GC** and **GS** cases (see Fig. 3). Collocation of negative $\overline{w'w'w'}$ with alternating-sign $\overline{\theta'\theta'\theta'}$ moments also points to rather different localization properties of velocity and temperature turbulent fluctuations within the entrainment zone.

Additionally, the upward transport of vertical velocity fluctuations throughout most of the CBL may explain the different effects of the **GS** and **GC** cases on the turbulence in the interior of the CBL. In the **GS** case, the shear is concentrated more across the CBL top, and because $\overline{w'w'w'}$ is never strongly negative in the CBL, the shear-generated turbulence remains isolated in the upper portions of the CBL. In the **GC** case, the positive $\overline{w'w'w'}$ transports the surface shear-generated turbulence upward, so the turbulence regime is modified throughout the interior of the CBL as well as at the top, where shear production of turbulence also occurs.

Profiles of the mean wind components for the cases **GC** and **GS** and the associated distributions of the x component of the vertical momentum flux are demonstrated in Fig. 6. Predictions of these flow characteristics by all the codes are qualitatively similar, although their magnitudes vary somewhat. The **NERSC** code predicts, in the **GC** case, a weaker vertical mixing of the x component of momentum and slightly larger magnitude of the y component of the mean wind compared to other codes. **NERSC** results for the **GS** case are not yet available.

6. CBL GROWTH

At the early stages of the CBL development, the overall turbulence regime of the CBL and the properties of entrainment, in particular, depend mostly on the method of convection initiation applied in the LES. Differences among the CBL depth values predicted by different codes for the **NS** case at t<2000s are illustrative of such a dependence, see Fig. 7. With increasing time, all codes predict the **NS**-case CBL to reach an equilibrium entrainment regime. As formulated in Fedorovich et al. (2004), this regime is realized when both the time rate of change of the CBL-mean turbulence kinetic energy and the energy drain from the CBL top become negligibly small.

There are certain differences between predictions of the CBL depth z_i in the equilibrium regime by different codes. One may notice, however, that all codes consistently predict larger z_i values when the CBL depth is determined from the elevation of the strongest temperature gradient (maximum inversion) than in the cases when z_i is estimated from the height of the kinematic heat flux minimum within the entrainment layer. The fact that the temperature-gradient method yields larger CBL depth values than the heat flux minimum approach, at least for the shear-free CBL, is rather well known. It has been reflected upon, for instance, in Sullivan et al. (1998) and Fedorovich et al. (2004). On the other hand, the temperature-gradient method provides a smoother dependence of z_i on t as compared to z_i determined from the statistically less

steady heat-flux data. For the equilibrium-regime z_i defined by the heat-flux method, an analytical zero-order model solution reads:

$$z_i = [2(1+2C_1)B_s t]^{1/2} N^{-1}, \qquad (1)$$

where B_s is the surface buoyancy flux, N is the Brunt-Väisälä (buoyancy) frequency in the free atmosphere above the CBL, and C_1 is an empirical constant representing the entrainment heat flux ratio in the zero-order model of equilibrium entrainment (Zilitinkevich 1991). The commonly adopted value of C_1, based on numerous estimates from atmospheric, oceanic, and laboratory data, is 0.2.

In the right-hand plot of Fig. 7, LES predictions of z_i (t) for the **NS** case are compared with the zero-order model solution (1). Generally, all the codes yield z_i (t) following the analytical 1/2 power law at large t rather well, and predictions by several codes match expression (1) with C_1=0.2 almost perfectly.

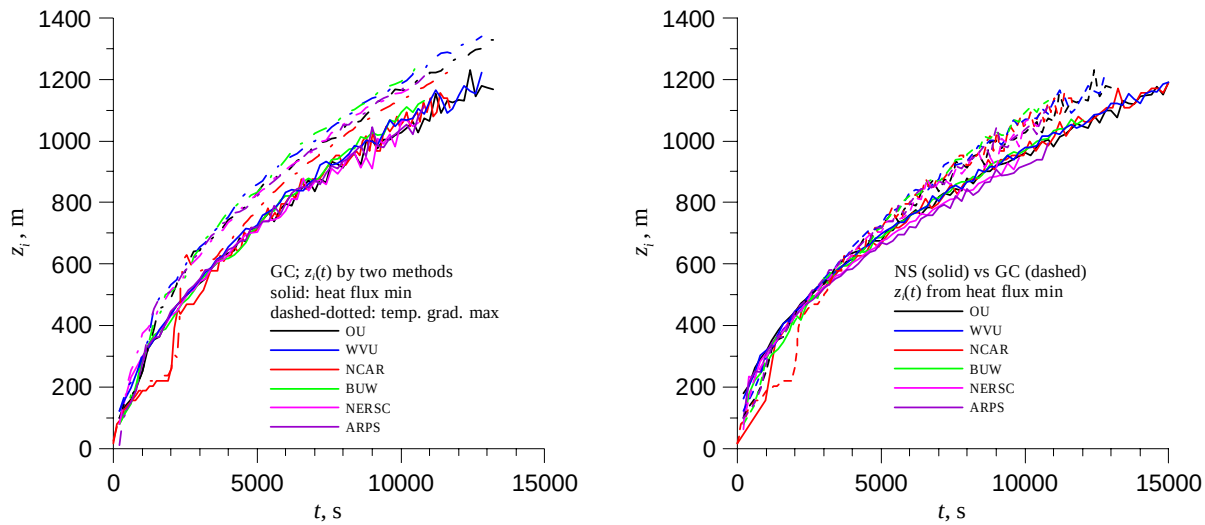

Figure 8. Evolution of the CBL depth in the **GC** case. In the left-hand plot: z_i (t) determined by two methods. In the right-hand plot: z_i (t) determined from the heat-flux minimum compared with its **NS** case counterpart.

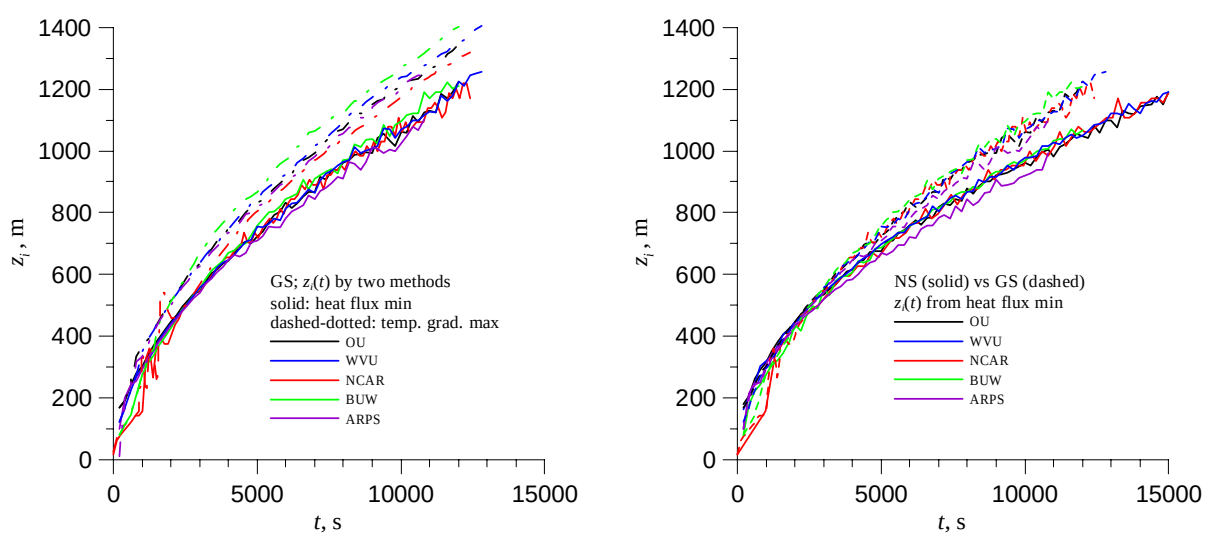

Figure 9. Evolution of the CBL depth in the **GS** case. In the left-hand plot: z_i (t) determined by two methods. In the right-hand plot: z_i (t) determined from the heat-flux minimum compared with its **NS** case counterpart.

In Fig. 8, we present the comparison of the LES predictions of $z_i(t)$ for the **GC** and **NS** cases. Comparison results for **GS** and **NS** cases are illustrated in Fig. 9. As one may notice, for **GC** and **GS** cases, all LES codes predict larger differences between CBL depths determined by the temperature-gradient and heat-flux methods. It is also clear that in both cases with wind shears (**GC** and **GS**), CBLs grow considerably faster than in the absence of mean wind shear (**NS** case).

Individually, the codes are notably consistent in predictions of the CBL growth as related to the intensity of entrainment. For instance, codes that predict stronger entrainment heat flux (see Fig. 3) also tend to predict faster CBL growth. Predictions by the **BUW** code, which yields the largest entrainment flux values in Fig. 3 and the fastest CBL growth in Figs. 7-9, may serve as the most illustrative example of such a consistency.

The large sensitivity of the overall CBL growth rate to the predictions of subgrid turbulence is probably an indication that the simulations are not resolving the shear-generated turbulence in the entrainment zone very well. The shear-generated turbulence may have smaller length scales, particularly in the **GS** case. Additionally, it should be taken into account that numerical damping occurring in some codes is much stronger for smaller-wavelength turbulent fluctuations.

7. SUMMARY AND CONCLUSIONS

In this study, modifications of entrainment in the CBL caused by wind shears have been analyzed, and shear-induced alterations of turbulence statistics of different kinds have been demonstrated. All LES codes in the comparison exercise have indicated that wind shears in the CBL and across the entrainment zone:

(***i***) induce vertical transport of heat and momentum in the upper portion of the CBL,

(***ii***) modify the turbulence regime in large portions of the CBL, particularly in the entrainment zone, but also throughout the depth of the CBL when large surface shear exists,

(***iii***) lead to deeper regions of negative heat flux (entrainment zones) at the CBL top, and

(***iv***) enhance convective entrainment and accelerate boundary-layer growth compared to the shear-free CBL.

Differences among the individual code-predicted CBL turbulence statistics have been found to increase with the order of statistics but have not shown noticeable dependence on wind shear. Apparently, for statistics of third order and higher, even the rather large sample size of about 250×250 (characteristic of the present study) does not provide sufficiently steady estimates. However, the basic features of the third-order turbulence moments in the simulated CBL have been captured by all codes in a common manner.

Further analyses of results from the LES comparison study of sheared CBLs are currently underway. In these analyses, the emphasis is laid on the self-similarity features of the CBL entrainment regimes under the influence of wind shears and development of approaches for their parameterization.

Acknowledgements: Authors gratefully acknowledge support by the National Science Foundation (Evgeni Fedorovich and Robert Conzemius – from grant ATM-0124068 and Fotini Katopodes Chow – from grant ATM-0073395) and by the Office of Naval Research (David Lewellen – from grant N00014-98-1-0595). The **BUW** simulations were conducted at SARA with financial support of NCF (project SG-132).

Conzemius, R., and E. Fedorovich, 2002: Dynamics of convective entrainment in a heterogeneously stratified atmosphere with wind shear. *Proc. 15th AMS Symp. on Boundary Layers and Turbulence*, 15-19 July 2002, Wageningen, the Netherlands, 31-34.

Cuijpers, J. W. M., and P. G. Duynkerke, 1993: Large eddy simulation of trade wind cumulus clouds. *J. Atmos. Sci.,* **50,** 3894–3908.

——, and A. A. M. Holtslag, 1998: Impact of skewness and nonlocal effect on scalar and buoyancy fluxes in convective boundary layers. *J. Atmos. Sci.,* **55,** 151–162.

Deardorff, J. W., 1980: Stratocumulus-capped mixed layers derived from a three-dimensional model. *Bound.-Layer Meteor.*, **18**, 495-527.

Esau, I., 2004: Simulation of Ekman boundary layers by large eddy model with dynamic mixed subfilter closure. *J. Env. Fluid Mech.*, **4**, 273-303.

Fedorovich, E., R. Conzemius, and D. Mironov, 2004: Convective entrainment into a shear-free linearly stratified atmosphere: bulk models reevaluated through large eddy simulations. *J. Atmos. Sci.*, **61**, 281-295.

——, F. T. M. Nieuwstadt, and R. Kaiser, 2001a: Numerical and laboratory study of horizontally evolving convective boundary layer. Part I: Transition regimes and development of the mixed layer. *J. Atmos. Sci.*, **58**, 70-86.

——, F. T. M. Nieuwstadt, and R. Kaiser, 2001b: Numerical and laboratory study of horizontally evolving convective boundary layer. Part II: Effects of elevated wind shear and surface roughness. *J. Atmos. Sci.*, **58**, 546-560.

Hunt, J. C. R., and P. A. Durbin, 1999: Perturbed vortical layers and shear sheltering. *Fluid Dyn. Res.*, **24**, 375-404.

Lewellen D. C., and W. S. Lewellen, 1998: Large-eddy boundary layer entrainment. *J. Atmos. Sci.*, **55**, 2645-2665.

Moeng, C.-H., 1984: A large-eddy simulation for the study of planetary boundary layer turbulence. *J. Atmos. Sci.*, **41**, 2052-2062.

Pino, D., J. Vilà-Guerau de Arellano, and P. Duynkerke, 2003: The contribution of shear to the evolution of a convective boundary layer. *J. Atmos. Sci.*, **60**, 1913-1926.

Sullivan, P., C.-H. Moeng, B. Stevens, D. H. Lenschow, and S. D. Mayor, 1998: Structure of the entrainment

zone capping the convective atmospheric boundary layer. *J. Atmos. Sci.*, **55**, 3042-3064.

Sykes, R. I., and D. S. Henn, 1989: Large-eddy simulation of turbulent sheared convection. *J. Atmos. Sci.*, **46**, 1106-1118.

Vreman, B., B. Geurts, and H. Kuerten, 1994: On the formulation of the dynamic mixed subgrid-scale model. *Phys. Fluids*, **6**, 4057-4059.

Xue, M., K. K. Droegemeier, and V. Wong, 2000: The advanced regional prediction system (ARPS) – a multi-scale nonhydrostatic atmospheric simulation and prediction model. Part I: Model dynamics and verification. *Meteorol. Atmos. Phys.*, **75**, 161-193.

——, K. K. Droegemeier, V. Wong, A. Shapiro, K. Brewster, F. Carr, D. Weber, Y. Liu, and D. Wang, 2001: The advanced regional prediction system (ARPS) – a multi-scale nonhydrostatic atmospheric simulation and prediction model. Part I: Model physics and applications. *Meteorol. Atmos. Phys.*, **76**, 143-65.

Zilitinkevich, S. S., 1991: *Turbulent Penetrative Convection*. Avebury Technical, Aldershot, 179 pp.